Flow pattern transition accompanied with sudden growth of flow resistance in two-dimensional curvilinear viscoelastic flows

Hiroki Yatou*

Department of Physics, Graduate School of Science, Kyoto University, Kyoto 606-8502, Japan

(Received 27 March 2010; revised manuscript received 5 July 2010; published 14 September 2010)

We numerically find three types of steady solutions of viscoelastic flows and flow pattern transitions between them in a two-dimensional wavy-walled channel for low to moderate Weissenberg (Wi) and Reynolds (Re) numbers using a spectral element method. The solutions are called "convective," "transition," and "elastic" in ascending order of Wi. In the convective region in the Wi-Re parameter space, convective effect and pressure gradient balance on average. As Wi increases, elastic effect becomes comparable, and the first transition sets in. Through the transition, a separation vortex disappears, and a jet flow induced close to the wall by the viscoelasticity moves into the bulk; the viscous drag significantly drops, and the elastic wall friction rises sharply. This transition is caused by an elastic force in the streamwise direction due to the competition of the convective and elastic effects. In the transition region, the convective and elastic effects balance. When the elastic effect becomes greater than the convective effect, the second transition occurs but it is relatively moderate. The second transition seems to be governed by the so-called Weissenberg effect. These transitions are not sensitive to driving forces. By a scaling analysis, it is shown that the stress component is proportional to the Reynolds number on the boundary of the first transition in the Wi-Re space. This scaling coincides well with the numerical result.

DOI: 10.1103/PhysRevE.82.036310 PACS number(s): 47.50.−d, 47.54.−r

I. INTRODUCTION

Nonlinearity due to viscoelasticity induces nontrivial flow behaviors such as rod climbing, secondary flows, and tubeless siphon in viscoelastic fluids [1]. The viscoelasticity is effective typically in polymeric fluids even though the amount of polymer additives is very small. For decades, many researchers have investigated such nontrivial flows from both academic and industrial standpoints.

The nonlinearity is often caused by the coupling between elastic stress and strain. The coupling is typically observed in rod climbing, i.e., the Weissenberg effect [2]. Rod climbing is caused by elastic stress acting in the centripetal direction of curved streamlines (called "hoop stress"). When a rod is rotated in a polymeric fluid, the rotating rod causes a shear flow. Because the shear flow stretches polymer molecules along streamlines, the elastic stress works in the inward direction of the streamlines by the tension of elongated polymer molecules. Then, the fluid is transferred in the inward direction, and finally climbs up along the rod.

The hoop stress often causes elastic instability. In Taylor-Couette flows, a radial velocity perturbation induces an additional hoop stress, and the hoop stress further amplifies the radial perturbation [3,4]. The elastic instability is followed by the formation of flow patterns including Taylor-Couette vortices, rotating standing waves, disordered oscillations, and solitary vortices between cylinders with increasing shear rate [4–7]. Elastic instabilities in curvilinear shear flows have been also observed in Taylor-Dean flow [8], cone-and-plate flow [9], and lid-driven cavity flow [10]. The elastic instability is caused even at very low Reynolds number $\mathrm{Re} \ll 1$. In this regime, elasticity-induced turbulence has also been observed in experiments [11–13]. The elastic turbulence is characterized by increased flow resistance and efficient mixing at very low Reynolds number [14]. The mixing in microdevices and nanodevices is an important industrial application of the elastic turbulence at $\mathrm{Re} \ll 1$ [15].

Our goal is the understanding of detailed mechanisms of flow pattern formation, elastic instability, and elastic turbulence in viscoelastic curvilinear channel flows employed in the experiments of elastic turbulence [12,14,16]. To this end, we perform numerical simulations of two-dimensional wavy-walled channel flows with a high-accuracy spectral element method, although earlier computations have mainly treated more simple flows such as Taylor-Couette flows and two-dimensional flows driven by external forcing with doubly periodic boundary conditions [7,17,18]. In this study, we investigate the flow patterns such as separation vortices and jet flows. We focus on an elastic force in the streamwise direction as a generation mechanism of the flow patterns, although the previous studies have basically deal with hoop stresses. Note that the streamwise elastic force is effective only when inertial effect is not negligible unlike the elastic instability at $\mathrm{Re} \ll 1$. In other words, the competition of the convective and elastic effects is essential for the flow pattern transition in the curvilinear shear flows.

In this study, we investigate base laminar steady solutions for low to moderate Reynolds and Weissenberg numbers. Note that Newtonian flows in the wavy-walled channel are linearly unstable at moderate Re [19] unlike two-dimensional Taylor-Couette and Taylor-Dean flows of viscoelastic fluids [20,21]. This may indicate that viscoelastic flows are also linearly unstable in wavy-walled channels. We expect that the study of the base solutions leads to investigations on elastic instability in future.

This paper is organized in the following way. In Sec. II, we show governing equations and nondimensional param-

*sanmaya@kyoryu.scphys.kyoto-u.ac.jp

eters. The numerical method, boundary conditions, parameters, the validation of our computations, and flow geometry are described in Sec. III. In Sec. IV, we show the main results, that is, the flow pattern transition and its mechanism. Section V is devoted to discussion and concluding remarks.

II. BASIC EQUATIONS

The governing equations of viscoelastic flows consist of the incompressible Navier-Stokes equation and a constitutive equation. In this study, we employ the FENE-P (finitely extensible nonlinear elastic-Peterlin) model as the constitutive equation. Then the governing equations are written in the following dimensionless form:

$$\nabla \cdot \boldsymbol{u} = 0, \tag{1}$$

$$\mathrm{Re}\left[\frac{\partial \boldsymbol{u}}{\partial t} + (\boldsymbol{u}\cdot\nabla)\boldsymbol{u}\right] = -\nabla p + \beta\nabla^2\boldsymbol{u} + \nabla\cdot\boldsymbol{\tau}, \tag{2}$$

$$\mathrm{Wi}\left[\frac{\partial \boldsymbol{C}}{\partial t} + (\boldsymbol{u}\cdot\nabla)\boldsymbol{C} - (\nabla\boldsymbol{u})^T\cdot\boldsymbol{C} - \boldsymbol{C}\cdot(\nabla\boldsymbol{u}) - \kappa\Delta\boldsymbol{C}\right] + [f(r)\boldsymbol{C} - \boldsymbol{I}] = 0, \tag{3}$$

$$\boldsymbol{\tau} = \frac{1-\beta}{\mathrm{Wi}}[f(r)\boldsymbol{C} - \boldsymbol{I}], \tag{4}$$

$$f(r) = \frac{K}{1 - \mathrm{Tr}(\boldsymbol{C})/L^2}, \quad K = 1 - 3/L^2, \tag{5}$$

where $\boldsymbol{u}$ is the velocity, p is the pressure, $\boldsymbol{\tau}$ is the extra-stress tensor, $\boldsymbol{C}$ is the conformation tensor, and L is the maximum polymer length. The velocity $\boldsymbol{u}$, coordinates $\boldsymbol{x}$, pressure p, elastic stress $\boldsymbol{\tau}$, and time t are scaled with the following characteristic quantities: U_0, L_0, $P_0 = \eta U_0/L_0$, $T_0 = \eta U_0/L_0$, and $t_0 = L_0/U_0$, respectively [22,23], where $\eta = \eta_s + \eta_p$ is the total viscosity defined as the sum of the solvent viscosity η_s and the polymer viscosity η_p. In this study, L_0 is a channel width, and U_0 is a tangential wall velocity of the bottom wall [see Fig. 1(a)].

These equations include the following nondimensional parameters: the Reynolds number, the Weissenberg number, and the viscosity ratio parameter. The Reynolds number is the ratio of inertial forces to viscous forces and is defined in the following way:

$$\mathrm{Re} = \rho U_0 L_0/\eta, \tag{6}$$

where ρ is the fluid density. The Weissenberg number is the ratio of the polymer relaxation time λ to the typical flow time t_0:

$$\mathrm{Wi} = \lambda/t_0. \tag{7}$$

The viscosity ratio parameter is the ratio of the solvent viscosity to the total viscosity:

$$\beta = \eta_s/\eta. \tag{8}$$

The FENE-P model is derived from a kinetic theory [24] and a preaveraging closure approximation [25] concerning elastic dumbbells consisting of two beads and a spring connecting them. The conformation tensor $\boldsymbol{C}$ is a measure of the second-order moment of the end-to-end distance vector $\boldsymbol{r}$ of dumbbells:

$$C_{ij} = \langle r_i r_j \rangle. \tag{9}$$

The function $f(r)$ in Eq. (5) is the so-called Peterlin function, which restricts the length of dumbbells to values less than the maximum length L. Because the FENE-P model qualitatively well reproduces the properties of viscoelastic flows (e.g., shear thinning [26,27]), the model has been frequently used in many studies of viscoelastic fluids [7,28–30].

We add an artificial diffusive term $\kappa\nabla^2\boldsymbol{C}$ in the constitutive equation (3) in order to avoid numerical instabilities, where κ is the artificial constitutive diffusivity coefficient. The additional diffusive term physically originates from the Brownian motion of the center of mass of elastic dumbbells across streamlines [31]. Sureshkumar and Beris investigated how the diffusive term influences flow stabilities in detail [32]. They concluded that a sufficiently small artificial diffusivity coefficient ($\kappa \leq 10^{-3}$) does not affect critical eigenmodes of a viscoelastic Orr-Sommerfeld problem, although the artificial diffusivity coefficient needed for numerical stabilization is much larger than the physically expected diffusivity. This indicates that a sufficiently small artificial diffusivity does not qualitatively change flow behaviors on numerical instability. Hence, the modification has been widely used in viscoelastic flow calculations using the FENE-P and other models [18,33].

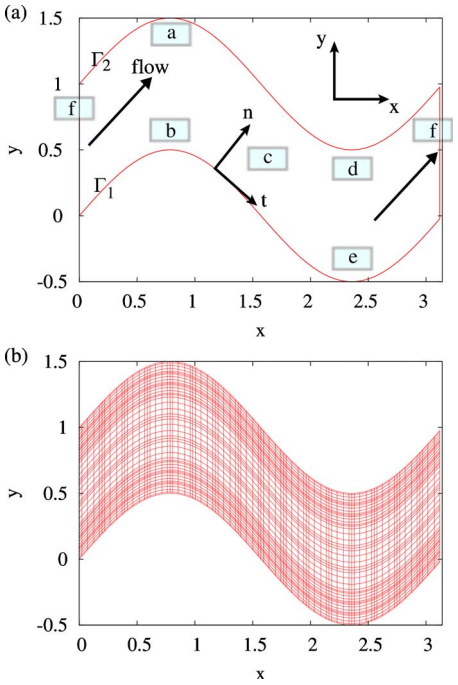

FIG. 1. (Color online) (a) Flow domain with symbols employed in this paper. Regions "a" and "e" are the outward regions. Regions "b" and "d" are the inward regions. Regions "c" and "f" are the contraction regions. Symbols "t" and "n" denote the directions tangential and normal to the boundary wall, respectively. (b) Computational mesh used in this study.

III. NUMERICAL METHOD

A. Spectral element methods

We use a spectral element method (hereinafter referred to as SEM) to discretize the governing equations in space [34–36]. SEM enables high-accuracy computations in complex geometries. In SEM, a computed domain is subdivided into several spectral elements. The values of the variables and the derivatives of the variables are interpolated using Lagrange polynomial interpolation functions [37]. Numerical errors between numerical solutions and exact solutions are reduced in the following two ways in SEM. First, the increase in the number of elements leads to an algebraic convergence of numerical accuracy. Second, the increase in the polynomial degree of interpolation functions results in an exponential convergence of numerical accuracy for sufficiently smooth solutions [38].

A Galerkin discretization is used in SEM. The weak form of the differential equations (1)–(4) is written as follows:

$$\int_{\Omega} (\nabla \cdot \boldsymbol{u}) q d\Omega = 0, \tag{10}$$

$$\mathrm{Re}\int_{\Omega} \frac{\partial \boldsymbol{u}}{\partial t} \cdot \boldsymbol{w} d\Omega + \mathrm{Re}\int_{\Omega} [(\boldsymbol{u} \cdot \nabla)\boldsymbol{u}] \cdot \boldsymbol{w} d\Omega - \int_{\Omega} p(\boldsymbol{I}:\nabla \boldsymbol{w}) d\Omega + \beta \int_{\Omega} (\nabla \boldsymbol{u}:\nabla \boldsymbol{w}) d\Omega + \int_{\Omega} \boldsymbol{\tau}:(\nabla \mathbf{w}) d\Omega - \int_{\Gamma} [\{-p\boldsymbol{I} + \beta[\nabla \boldsymbol{v} + (\nabla \boldsymbol{v})^T] + \boldsymbol{\tau}\} \cdot \boldsymbol{n}] \cdot \boldsymbol{w} d\Gamma = 0, \tag{11}$$

$$\mathrm{Wi}\int_{\Omega} \left[\frac{\partial \boldsymbol{C}}{\partial t} + (\boldsymbol{u} \cdot \nabla)\boldsymbol{C} - [(\nabla \boldsymbol{u})^T \cdot \boldsymbol{C}] - \boldsymbol{C} \cdot (\nabla \boldsymbol{u}) \right] : \boldsymbol{S} d\Omega + \mathrm{Wi}\int_{\Omega} (\kappa \nabla \boldsymbol{C}):(\nabla \boldsymbol{S}) d\Omega + \int_{\Omega} [f(r)\boldsymbol{C} - \boldsymbol{I}]:\boldsymbol{S} d\Omega - \int_{\Gamma} (\nabla \boldsymbol{C} \cdot \boldsymbol{n}):\boldsymbol{S} d\Gamma = 0, \tag{12}$$

where the scalar product of two tensors $\boldsymbol{P}$ and $\boldsymbol{Q}$ is defined as

$$\boldsymbol{P}:\boldsymbol{Q} = P_{ij}Q_{ij}, \quad 1 \le i, \quad j \le 2, \tag{13}$$

and the notation $(\nabla \boldsymbol{u})_{ij} = \partial u_j / \partial x_i$ is adopted. The pressure p and the test function q belong to the functional space $Q \subset L^2(\Omega)$. The velocity $\boldsymbol{u}$ and the test function $\boldsymbol{w}$ belong to the space $W \subset H^1(\Omega)^2$. The conformation tensor $\boldsymbol{C}$ and the test function $\boldsymbol{S}$ belong to $\Sigma \subset H^1(\Omega)^{2\times 2}$. Here, $L^2(\Omega)$ and $H^1(\Omega)$ represent the space of square-integrable functions and the space of derivative functions whose first-order derivatives are square integrable on Ω, respectively.

In this study, we distribute more elements near walls as shown in Fig. 1(b) because the gradient of the elastic stress is larger there. In each element, we approximate the variables p, every direction of $\boldsymbol{u}$, and every component of $\boldsymbol{C}$ using Lagrange interpolants of the degrees N_p, N_u, and N_C, respectively. We set $N_u = N_C$ and set $N_p = N_u - 2$ in order to avoid the so-called spurious pressure oscillations [38]. In this condition, the pressure approximation is discontinuous. The test functions q, $\boldsymbol{w}$, and $\boldsymbol{S}$ are also approximated using the same interpolants as the corresponding variables p, $\boldsymbol{u}$, and $\boldsymbol{C}$, respectively. We do not employ any stabilization techniques such as SUPG (stream upwind/Petrov Galerkin) except the artificial diffusive term. We evaluate the integrals in Eqs. (10)–(12) with a quadrature rule and finally derive nonlinear algebraic equations with operator matrices and variable vectors.

The linear and nonlinear terms are discretized in time using a second-order backward difference scheme (BDF2) and a second-order extrapolation scheme (EX2), respectively. We adopt a decoupled approach to solve the temporal discretized algebraic equations [22,39,40].

B. Boundary conditions

No-slip boundary conditions are imposed on the velocity at the upper and bottom walls. Periodic boundary conditions are imposed on the velocity and the conformation tensor at the inflow and outflow boundaries. No pressure boundary conditions are imposed in our calculations as in the previous numerical studies using SEM and the decoupled method of the temporal discretization [22,39,40].

The boundary integrals in Eqs. (11) and (12) vanish for the following reasons. First, the boundary integrals in Eqs. (11) and (12) on the inflow and outflow boundaries are zero because of the periodicity. Second, the boundary integral in Eq. (11) on the walls becomes zero since the test function $\boldsymbol{w}$ is set to zero on such Dirichlet boundaries in SEM. Third, the boundary integral in Eq. (12) on the walls is set to zero in this study because our calculations with finite boundary integrals suffered numerical instabilities for $\mathrm{Wi} > 0.5$. However, at the low Weissenberg number $\mathrm{Wi} = 0.1$, we have confirmed that the flow patterns described in Sec. IV are not sensitive to whether the boundary integral is zero or finite.

We mainly investigate Couette-type flows in which the upper wall is at rest, and a constant speed is given on the bottom wall. The wall speed of the bottom wall is normalized to unity along the tangential direction t defined in Fig. 1(a) at every point on the bottom wall. We also investigate Poiseuille-type flows in which both the upper and bottom walls are at rest.

C. Parameters

In this section, we summarize the parameters used in this study: (1) flow and rheological parameters are the Reynolds number Re, the Weissenberg number Wi, the viscosity ratio parameter β, and the maximum dumbbell length L; (2) geometric parameters are the wall amplitude A and the periodic length L_x defined in Sec. III E; and (3) the artificial diffusivity coefficient κ. We focus on the dependence of flow behaviors on the Reynolds and Weissenberg numbers. The other parameters β, L, κ, and L_x are fixed to the values shown in Table I. We fix the wall amplitude A to 0.5 in Couette-type flow calculations and to 0.3 in Poiseuille-type flow ones. We set the maximum dumbbell length L to the sufficiently large value $L^2 = 1.0 \times 10^4$ in order to capture the influence of large

TABLE I. Number of elements N_{el}, polynomial degree of the velocity N_u, and parameter values fixed in our computations. In the case of $N_u=6$, N_p and N_C are set to 4 and 6, respectively.

N_{el}	N_u	L_x	β	L^2	κ
192	6	π	0.5	1.0×10^4	1.0×10^{-3}

elastic stress on flows. The values of the fixed parameters β, L, and κ have been frequently used in the previous numerical studies of viscoelastic flows [7,18,32,33]. Our several test runs show that these parameter values do not qualitatively influence flow behaviors. Moreover, we also performed calculations with different numbers of elements and polynomial degrees: (1) $N_{el}=72$ and $N_u=6$, (2) $N_{el}=240$ and $N_u=6$, and (3) $N_{el}=192$ and $N_u=8$. We found that the results of this study, flow pattern transitions and the critical Weissenberg numbers, do not depend on meshes.

D. Validation of our computations

The validation of our numerical code is carried out by the comparison of numerical and exact solutions of plane-Couette flows. We perform calculations at the low Weissenberg number Wi=1.0 with zero artificial diffusivity coefficient $\kappa=0$ and at the high Weissenberg number Wi=20.0 with the finite artificial diffusivity coefficient $\kappa=1.0\times10^{-3}$.

The exact solutions of plane-Couette flows of the FENE-P model are derived as the roots of the following equations (14) and (15) obtained from the original equations under the conditions that the derivatives of all variables with respect to x are zero, $p=$const, $u_x=1-y$, and $u_y=0$:

$$2\,\mathrm{Wi}^2\,C_{yy}^3+(L^2K+2)C_{yy}-L-2=0, \tag{14}$$

$$C_{xy}+\mathrm{Wi}\,C_{yy}^2=0, \quad C_{xx}-L^2+(L^2K+1)C_{yy}=0. \tag{15}$$

The conformation tensor $\boldsymbol{C}$ and the elastic stress $\boldsymbol{\tau}$ of the exact solutions are uniform in the whole domain. We calculate the extra-stress components for the validation of our computations.

Table II shows numerical errors of our computations with the several parameter values. The numerical error of the extra-stress component τ_{xx} is defined as $\tau_{xx}^{err}=|(\tau_{xx}^{cal}-\tau_{xx}^{ex})/\tau_{xx}^{cal})|$, where τ_{xx}^{cal} and τ_{xx}^{ex} are the values of the extra-stress components of our computation and the exact solution, respectively. The numerical error of the stress component τ_{xy} is defined in the same way. Because τ_{yy} of the exact solution is zero, we use the absolute value of τ_{yy}^{cal} as the numerical error of τ_{yy}. The numerical errors are within 10^{-4} for the wide range of parameter values. Moreover, numerical accuracy is improved with mesh refinements.

E. Flow geometry

The governing equations are solved in the domain sketched in Fig. 1(a). Two sinusoidal curves are boundary walls. The coordinates of the upper and bottom walls are defined as follows:

$$\Gamma_1(\mathrm{bottom}):y=A\,\sin(2\pi x/L_x),$$

$$\Gamma_2(\mathrm{upper}):y=1+A\,\sin(2\pi x/L_x),$$

where A is the amplitude of wall corrugations and L_x is the length of the periodic channel in the direction of x. The channel width is normalized to unity. We call this channel "sinuous channel" as used by Cho *et al.* [19]. We call regions "a" and "e" in Fig. 1(a) "outward region" because these regions are located in the outward positions of curved flows. We similarly call regions "b" and "d" in Fig. 1(a) "inward region." Regions "c" and "f" in Fig. 1(a) are called "contraction region." Symbols "t" and "n" denote the directions tangential and normal to the walls, respectively.

We adopt the sinuous channel in this study for the following reasons. First, the channel has mixed kinematics with both shear and extensional flows. The elastic stress augmented by dumbbell stretching in these flows strongly influences flow behaviors. Second, we can easily control the magnitude of shear and extension by changing the wall amplitude A and the periodic length L_x. Third, streamlines are highly curved in this channel. The curvature of streamlines locally varies, and the sign of the curvature is even reversed along the streamlines unlike two-dimensional Taylor-Couette flows in which the sign of the curvature is not changed along streamlines. The spatial variation of the curvature directly changes the magnitude and the direction of the hoop stress.

TABLE II. Numerical errors of the components of the extra-stress tensor. $\tau_{xx}^{err}=|(\tau_{xx}^{cal}-\tau_{xx}^{ex})/\tau_{xx}^{cal})|$ is the numerical error of τ_{xx}, where τ_{xx}^{cal} and τ_{xx}^{ex} are the values of the extra-stress component of our computation and the exact solution, respectively.

N_{el}	N_u	Wi	L^2	κ	τ_{xx}^{err}	τ_{xy}^{err}	$\lvert\tau_{yy}^{cal}\rvert$
48	4	1.0	10.0	0.0	4.7×10^{-5}	2.3×10^{-5}	3.5×10^{-7}
192	6	1.0	10.0	0.0	2.6×10^{-5}	1.3×10^{-5}	4.2×10^{-9}
48	4	1.0	1.0×10^4	0.0	5.3×10^{-5}	2.7×10^{-5}	3.0×10^{-7}
192	6	1.0	1.0×10^4	0.0	3.0×10^{-5}	1.5×10^{-5}	1.6×10^{-9}
48	4	20.0	1.0×10^4	1.0×10^3	3.4×10^{-5}	2.4×10^{-5}	5.6×10^{-7}
192	6	20.0	1.0×10^4	1.0×10^3	2.9×10^{-5}	1.6×10^{-5}	1.1×10^{-8}

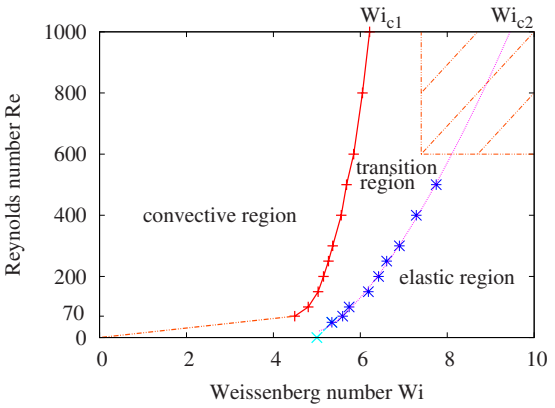

FIG. 2. (Color online) Phase diagram of the steady solutions in the plane of Wi and Re. The left and right curves denote the first and second critical Weissenberg numbers, Wi_{c1} and Wi_{c2}, respectively. The Reynolds number of the bottom edge of the left solid curve Re=70 is determined through the scaling analysis in Sec. IV E. The right curve is extrapolated to a large-Re region using a fitting function. The value of Wi_{c2} at Re=0 is the Weissenberg number at which the separation vortex emerges. In the region with diagonal lines, our calculations suffer numerical instabilities.

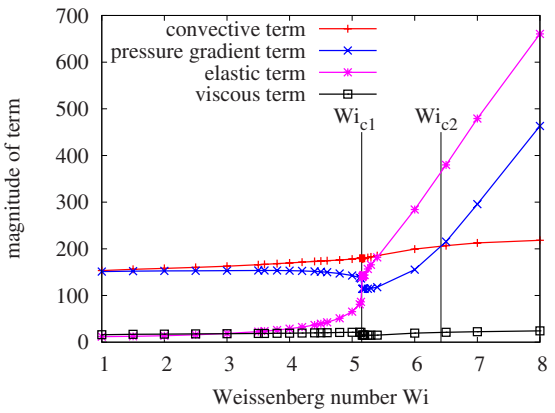

FIG. 3. (Color online) Magnitudes of the convective term $\|\mathrm{Re}(\boldsymbol{u}\cdot\nabla)\boldsymbol{u}\|$, the pressure-gradient term $\|\nabla p\|$, the elastic term $\|\nabla\cdot\boldsymbol{\tau}\|$, and the viscous term $\|\beta\nabla^2\boldsymbol{u}\|$ in the Navier-Stokes equation as functions of Wi at Re=200.

IV. RESULTS

A. Three types of steady solutions

We perform numerical simulations for the wide range of Weissenberg number $0\leq \mathrm{Wi}\leq 20$ and Reynolds number $0\leq \mathrm{Re}\leq 1000$. We numerically find three types of steady solutions. We call the steady solutions convective, transition, and elastic in ascending order of Wi. The three regions of the steady solutions in the Wi-Re parameter space are shown in Fig. 2. The adjacent regions are separated with two curves. We call the left curve the first critical Weissenberg number Wi_{c1} and call the right curve the second critical Weissenberg number Wi_{c2}. Wi_{c2} is extrapolated to a large-Re region using a fitting function because our numerical calculations suffer numerical instabilities in the large-Wi and -Re regions denoted by diagonal lines in Fig. 2.

These critical Weissenberg numbers are defined in the following way. First, we estimate the magnitude of each term in the Navier-Stokes equation using the following quantity:

$$\|\mathrm{Re}(\boldsymbol{u}\cdot\nabla)\boldsymbol{u}\| = \int_{\Omega} |\mathrm{Re}(\boldsymbol{u}\cdot\nabla)\boldsymbol{u}|d\Omega. \tag{16}$$

Here, we define the absolute value $|\mathrm{Re}(\boldsymbol{u}\cdot\nabla)\boldsymbol{u}|$ in the following way:

$$|\mathrm{Re}(\boldsymbol{u}\cdot\nabla)\boldsymbol{u}| = \{[\mathrm{Re}(\boldsymbol{u}\cdot\nabla)u_x]^2 + [\mathrm{Re}(\boldsymbol{u}\cdot\nabla)u_y]^2\}^{1/2}. \tag{17}$$

This absolute value represents the magnitude of each term at each position in the domain Ω. The spatial integral of this absolute value is used as the magnitude of the term in the whole domain.

Figure 3 shows the magnitudes of the convective term $\|\mathrm{Re}(\boldsymbol{u}\cdot\nabla)\boldsymbol{u}\|$, the pressure-gradient term $\|\nabla p\|$, the elastic term $\|\nabla\cdot\boldsymbol{\tau}\|$, and the viscous term $\|\beta\nabla^2\boldsymbol{u}\|$ as functions of Wi at Re=200. We define Wi_{c1} as Wi at which the magnitudes of the elastic and pressure-gradient terms become the same value. Wi_{c2} is similarly defined as Wi at which the magnitudes of the pressure-gradient and convective terms become the same value.

B. Flow pattern transition

In this section, we show several flow patterns of the three types of steady solutions. Figure 4 shows typical streamlines in the convective, transition, and elastic regions at the moderate Reynolds numbers Re=200 and 400. In the convective region, the flow field consists of a bulk shear flow and a vortex in the outward region (a) [see the definition of the outward region (a) in Fig. 1(a)]. We call the vortex "separation vortex" because the vortex is detached from the bulk flow. The vortex becomes smaller with increasing Wi. At Wi_{c1}, that is the beginning of the transition region, the vortex vanishes or becomes significantly small. The separation vortex reappears and subsequently grows with further increasing Wi. The size of the vortex in the elastic region is close to that in the convective region.

Figure 5 shows the vertical cross sections of the velocity component u_x at $x=\pi/4$ at Re=200, 400, and 800. We define a "jet flow" as the region in which the velocity is larger than that in the surrounding region. Such jet flows are observed near the bottom wall $0.5<y<0.7$ in the convective region as shown in curves [a]–[c] in Figs. 5(a), 5(c), and 5(d). These jet flows disappear at Wi_{c1} as shown in curve [d] in Figs. 5(a), 5(c), and 5(d). Then, new jet flows emerge near the upper wall. These jet flows near the upper wall are broader than those in the convective region. These jet flows gradually approach the bottom wall with Wi through the transition region as shown in curves [d] and [e] in Figs. 5(a), 5(c), and 5(d). In the elastic region, the jet flows are present near the bottom wall again as shown in curve [f] in Figs. 5(a) and 5(c). The jet flows at each Re are basically similar in all the regions. However, the jet flows at larger Re are sharper and slightly more distorted in the transition region and are broader in the elastic region.

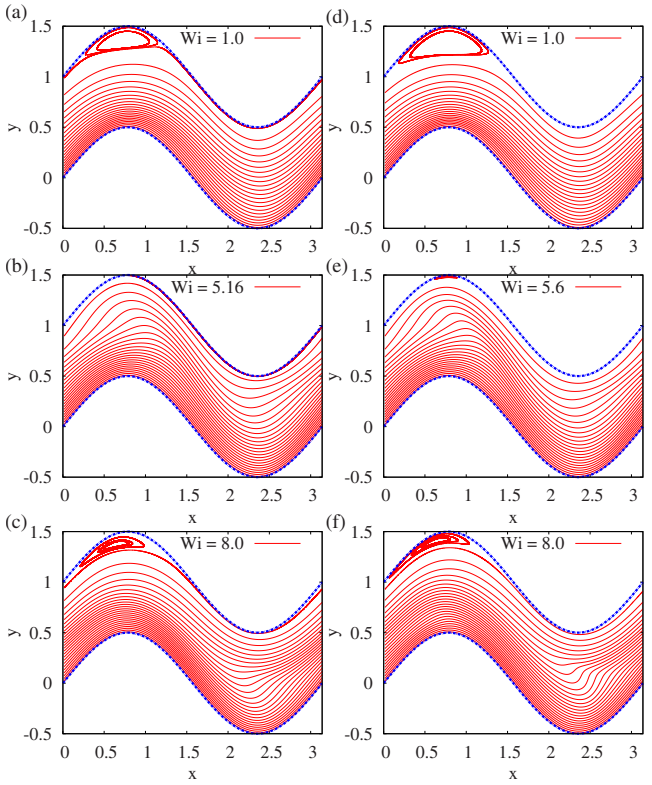

FIG. 4. (Color online) Streamlines of the steady solutions at (a)–(c) Re=200 and (d)–(f) Re=400. (a), (b), and (c) represent the streamlines in the convective region Wi=1.0, in the transition region Wi=5.16, and in the elastic region Wi=8.0, respectively. (d), (e), and (f) represent the streamlines in the convective region Wi =1.0, in the transition region Wi=5.6, and in the elastic region Wi=8.0, respectively. The streamlines are drawn using passively advected particles. The intervals of the streamlines in the bulk regions are inversely proportional to the flow speed, but the intervals of the streamlines in the separation vortices are independent of the flow speed.

In order to confirm that Wi_{c1} accords to Wi at which the pattern transition occurs, we calculate the maximum flow speed in the separation vortex as a strength of the separation vortex. The maximum speed is defined in the following way. We consider the region where $u_x<0$ in the separation vortex as shown in Figs. 4(a) and 5(b). We calculate the maximum value of the flow speed $|\boldsymbol{u}|$ in this region. When the separation vortex vanishes, the region where $u_x<0$ also disappears. Then, the maximum speed is set to zero. In Fig. 6, we show the maximum speed as a function of Wi at Re=100 and 200. This figure shows that Wi_{c1} coincides with Wi at which the separation vanishes. Wi_{c2} is close to Wi at which the jet flow reaches the bottom wall in the transition region. However, this estimate is less exact compared to the accordance of Wi_{c1} to Wi at which the separation vortex vanishes. We call the change of the flow patterns in the three regions "flow pattern transition."

C. Characteristics of flows

In the preceding sections, we show the three types of steady solutions and the two types of flow pattern transitions between them. The flow pattern transition is accompanied with the change of characteristic quantities of viscoelastic flows. In this section, we show the dependence of viscous wall friction, flow rate, and elastic wall friction on Wi.

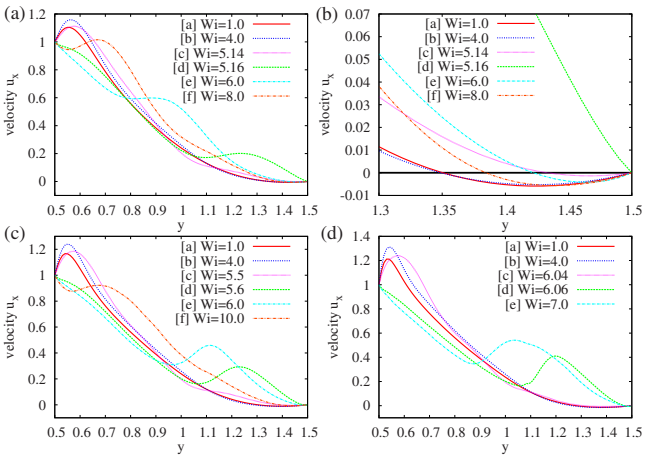

FIG. 5. (Color online) Velocity component u_x in the vertical cross section at $x=\pi/4$ at (a) and (b) Re=200, (c) Re=400, and (d) Re=800. In (a), the curves of the velocity component at [a] Wi =1.0, [b] Wi=4.0, [c] Wi=5.14 (convective region), [d] Wi=5.16, [e] Wi=6.0 (transition region), and [f] Wi=8.0 (elastic region) are drawn. In (b), the curves in (a) are magnified in $1.3\leq y\leq 1.5$. In (c), the curves of the velocity component at [a] Wi=1.0, [b] Wi=4.0, [c] Wi=5.5 (convective region), [d] Wi=5.6, [e] Wi=6.0 (transition region), and [f] Wi=10.0 (elastic region) are drawn. In (d), the curves of the velocity component at [a] Wi=1.0, [b] Wi=4.0, [c] Wi=6.04 (convective region), [d] Wi=6.06, and [e] Wi=7.0 (transition region) are drawn.

1. Laminar drag reduction

We define average viscous wall friction (viscous drag) acting on the walls of the channel as follows:

$$\tau_{vwf}=\frac{1}{S_\Gamma}\int_\Gamma \beta\left|\frac{\partial u_t}{\partial n}\right|d\Gamma, \tag{18}$$

where Γ is the sum of the bottom boundary Γ_1 and the upper boundary Γ_2, S_Γ is the sum of the lengths of the upper and

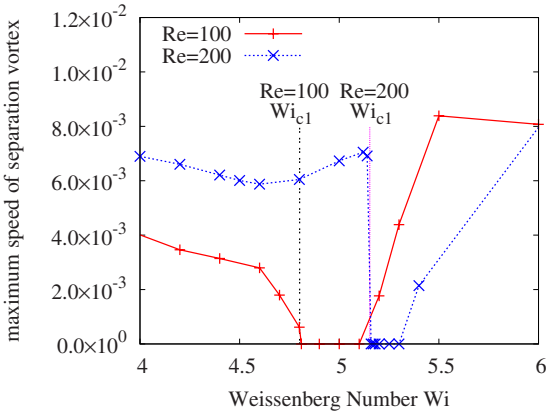

FIG. 6. (Color online) Maximum flow speed in the separation vortex as a function of Wi at Re=100 and 200. The vertical lines denote Wi_{c1} at Re=100 and 200.

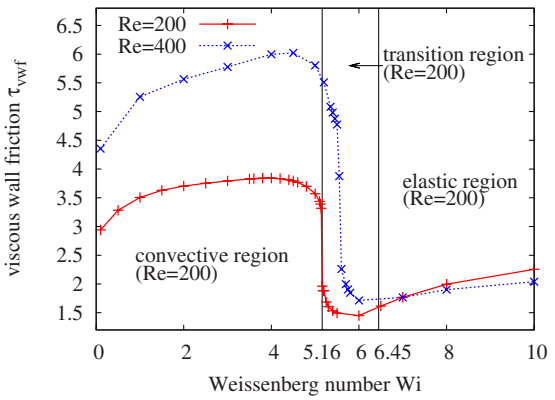

FIG. 7. (Color online) Average viscous wall friction τ_{vwf} as a function of Wi at Re=200 and 400. Two vertical lines represent Wi_{c1} and Wi_{c2} at Re=200.

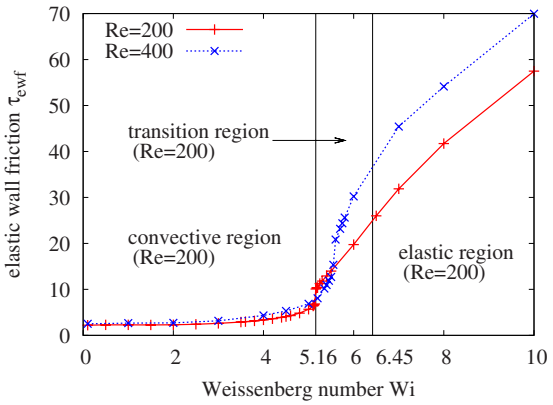

FIG. 9. (Color online) Average elastic wall friction τ_{ewf} as a function of Wi at Re=200 and 400. Two vertical lines represent Wi_{c1} and Wi_{c2} at Re=200.

bottom boundary walls, and the symbols t and n denote tangential and normal directions [see Fig. 1(a)]. Then $\partial u_t/\partial n$ represents the derivative of the tangential velocity component u_t with respect to the wall-normal direction n.

Figure 7 shows the average viscous wall friction as a function of Wi at Re=200 and 400. The viscous friction gradually grows in the convective region. The friction greatly decreases near Wi_{c1} and grows again in the elastic region. This shows that the viscous friction is reduced when the separation vortex vanishes. We call the drag reduction in laminar steady flows "laminar drag reduction" which has been also used in the studies of viscoelastic flows in curved circular pipes [41].

2. Flow rate

The flow rate FR in the channel is defined in the following way:

$$\mathrm{FR} = \int_0^1 u_x(\pi/2, y)dy. \tag{19}$$

Figure 8 shows the flow rate FR as a function of Wi at Re=200 and 400. In the convective region, the flow rate gradually increases. The flow rate temporarily decreases near Wi_{c1}

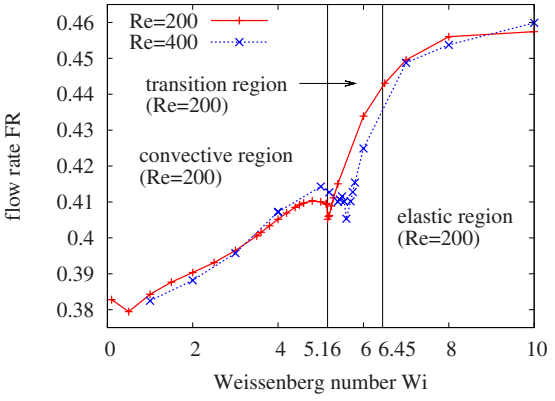

FIG. 8. (Color online) Flow rate FR as a function of Wi at Re=200 and 400. Two vertical lines represent Wi_{c1} and Wi_{c2} at Re=200.

but greatly grows in the transition region. In the elastic region, the growth of the flow rate is almost saturated.

3. Growth of flow resistance

We define average elastic wall friction as follows:

$$\tau_{ewf} = \frac{1}{S_\Gamma}\int_\Gamma \tau_{tn} d\Gamma, \tag{20}$$

where τ_{tn} is a component of the extra-stress tensor in the coordinate of two base vectors, a tangential unit vector (defined as $\boldsymbol{t}$), and a normal unit vector (defined as $\boldsymbol{n}$) as shown in Fig. 1(a). The elastic wall friction represents an additional flow resistance resulting from the elastic stress. The sum of the viscous and elastic wall frictions is a total flow resistance acting on the walls.

Figure 9 shows the average elastic wall friction as a function of Wi at Re=200 and 400. The elastic wall friction continuously increases with Wi, but the growth rate of the friction is very large at around Wi_{c1}. This shows that the elastic wall friction significantly grows when the pattern transition occurs.

D. Mechanism of flow pattern transition

In this section, we describe the mechanism of the flow pattern transition. Before the description, in Figs. 10 and 11, we show the contours of the pressure, the flow speed, and the trace of the conformation tensor $\mathrm{Tr}(\boldsymbol{C})$ in the convective, transition, and elastic regions at Re=200. The trace of the conformation tensor represents the magnitude of dumbbell stretching. Note that the pressure is fixed to zero at the given point. Negative pressure at a certain point then represents the pressure smaller than that at the reference point. In these figures, we can see the mutual relations among centrifugal (convective) force, elastic force, and pressure gradient. Here, the centrifugal force is defined as $\mathrm{Re}(u_t^2/R)$, where R is the curvature radius of streamline. Figure 12 schematically summarizes the transition of the force balance in the three regions. In the subsequent sections, we qualitatively describe the mechanism of the flow pattern transition in detail.

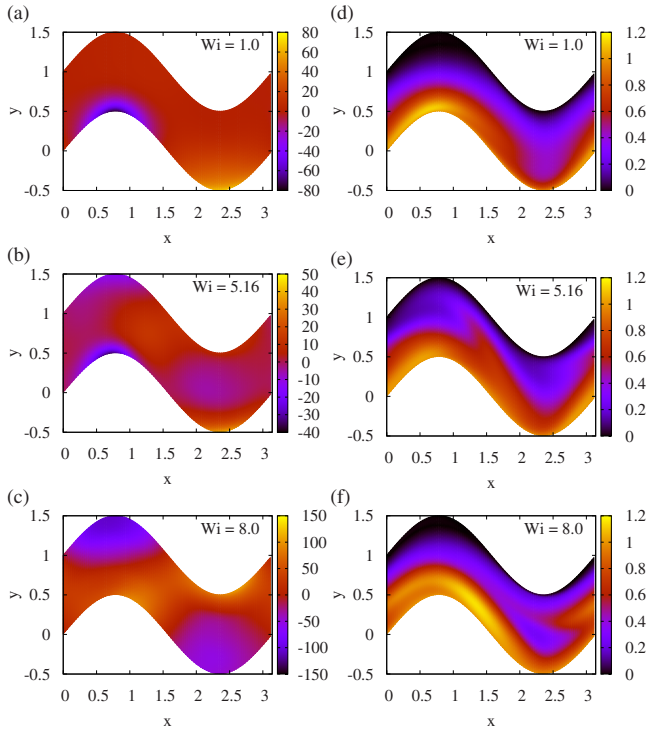

FIG. 10. (Color online) (a)–(c) Pressure and (d)–(f) flow-speed contours [(a) and (d)] in the convective region Wi=1.0, [(b) and (e)] in the transition region Wi=5.16, and [(c) and (f)] in the elastic region Wi=8.0 at Re=200.

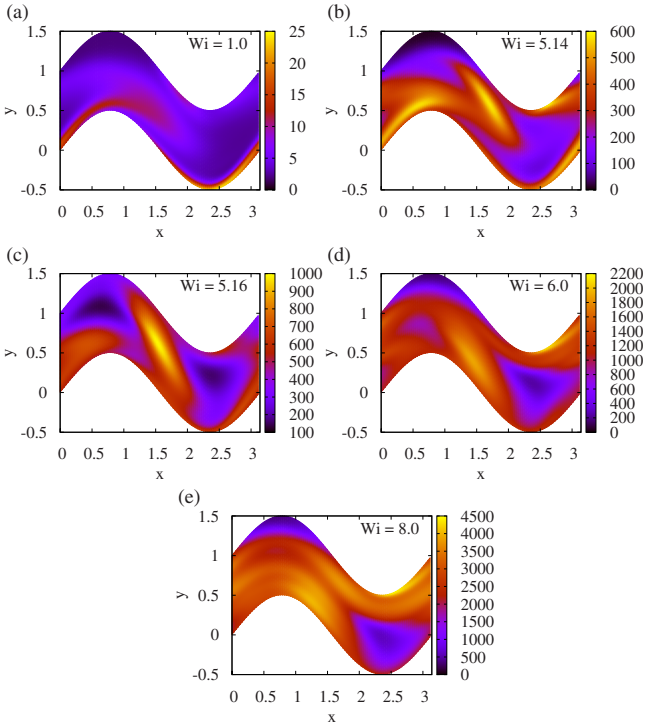

FIG. 11. (Color online) Contours of the trace of the conformation tensor Tr($\boldsymbol{C}$) in the convective region [(a) Wi=1.0 and (b) Wi=5.14], in the transition region [(c) Wi=5.16 and (d) Wi=6.0], and in the elastic region [(e) Wi=8.0] at Re=200.

1. Convective region

In the convective region, the separation vortex emerges in the outward region (a) [see Fig. 4(a)]. This is a characteristic phenomenon of Newtonian flows in wavy-walled channels [42]. On the other hand, the jet flow, which is a characteristic phenomenon of viscoelastic flows, is also observed in the inward region (b) despite a small Wi (see Fig. 10(d) and $0.5<y<0.7$ in curves [a]–[c] in Figs. 5(a), 5(c), and 5(d)).

The separation vortex is generated by the balance of the pressure gradient and the centrifugal force as follows. In the convective region, the magnitudes of the convective and pressure-gradient terms are almost the same as shown in Fig. 3. The centrifugal force is large particularly in the inward region (b) because both of the velocity and curvature are large there. The centrifugal force balances with a centripetal pressure gradient. In other words, the pressure becomes smaller in the inward region (b) than in the outward region (a) [see Fig. 10(a)]. The pressure gradient inhibits flows to the outward region (a), and thus the separation vortex detached from the bulk flow emerges in the outward region (a).

The jet flow is generated by streamwise elastic force. The bulk shear flow through the inward region (b) strongly enhances the elastic stress (or stretches elastic dumbbells) near the bottom wall. The enhanced elastic stress directly produces a streamwise elastic force, and the elastic force increases streamwise flows [see Fig. 11(a)]. Then, the jet flow emerges in the inward region (b).

The viscous drag gradually grows with Wi because the augmented jet flow increases the velocity gradient near the bottom wall. Then, the flow speed near the bottom wall increases, and the flow rate also grows.

At the end of the convective region, the elastic stress grows particularly in the contraction regions (c) and (f) [see Fig. 11(b)]. The velocity is larger in these regions than in the surrounding regions because the channel is narrower in these regions than in the surrounding regions, and the flow rate is constant in every wall-normal cross section. The velocity

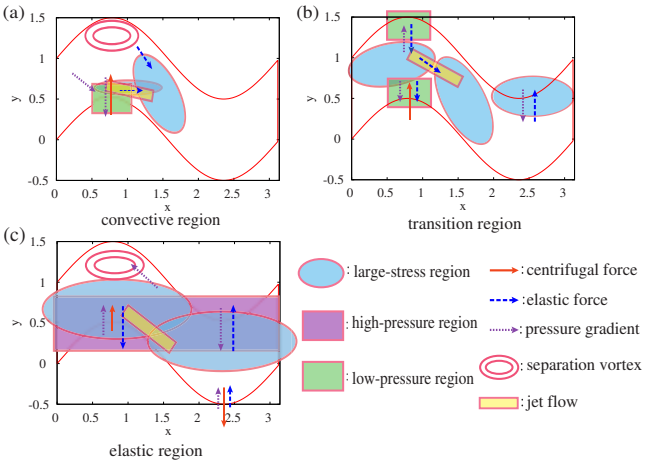

FIG. 12. (Color online) Schematics of force balance among the centrifugal force, the elastic force, and the pressure gradient in the (a) convective, (b) transition, and (c) elastic regions. The characteristic regions and flow patterns used in the description of the mechanism are superposed.

gradient stretches dumbbells in the streamwise direction and increases the elastic stress. Because the elastic stress in the contraction region (c) becomes larger than that in the outward region (a), the flow from the outward region (a) to the contraction region (c) is induced. Then, the separation vortex in the outward region (a) becomes small (see also curves [b] and [c] in Fig. 5(b)). The jet flow weakens, and the viscous drag decreases (see $0.5<y<0.7$ in curves [b] and [c] in Figs. 5(a), 5(c), and 5(d)) because the flow above the jet flow is enhanced by the elastic force near the contraction region (c).

This section is summarized as follows [see also Fig. 12(a)]. The separation vortex in the outward region (a) and the jet flow in the inward region (b) are the characteristic flow patterns of the steady solutions in the convective region. The separation vortex appears even in Newtonian flows, whereas the jet flow emerges only in viscoelastic flows.

2. Transition region

At the beginning of the transition region (i.e., at Wi_{c1}), the separation vortex in the outward region (a) and the jet flow in the inward region (b) disappear. Then, the jet flow near the outward region (a) emerges (see Fig. 10(e) and $1.1<y<1.5$ in curves [c] and [d] in Figs. 5(a), 5(c), and 5(d)).

These changes are the same phenomenon caused by the streamwise elastic force. The flow from the outward region (a) to the contraction region (c) gradually increases with Wi due to the elastic force. The increased flow further augments the elastic stress in the contraction region (c) because the increased velocity gradient further stretches elastic dumbbells. The additional elastic stress increases the flow again. This process greatly induces the flow and finally produces the jet flow in the outward region (a). Then, because the bulk flow passes through the outward region (a), the separation vortex disappears. The jet flow in the inward region (b) disappears due to the increase in the flow through the outward region (a), and then the viscous drag greatly drops as shown in Fig. 7. The growth rate of the flow rate increases above Wi_{c1} because the growth rate of the streamwise elastic force also becomes large (see Fig. 3). The enhanced stress in the contraction region (c) reaches the walls [see Fig. 11(c)]. Then, the elastic wall friction considerably rises as shown in Fig. 9.

Through the transition region, the jet flow in the outward region (a) gradually moves to the bottom wall with Wi (see curves [d]–[f] in Figs. 5(a) and 5(c)). This is because a hoop stress induces a flow in the centripetal direction in the outward region (a). This flow transfers the large-stress region in the contraction region (c) in the same direction [see Fig. 11(d)]. Then, the jet flow induced by the descending large-stress region also moves in the same direction (see curve [e] in Figs. 5(a), 5(c), and 5(d)). The jet flow gradually approaches the bottom wall with the hoop stress increasing. Then, the flow to the outward region (a) is reduced, and finally the separation vortex reappears there (see curves [d]–[f] in Fig. 5(b)).

Figure 10(b) shows that the pressure field follows these phenomena as follows. First, the centrifugal pressure gradient is present in the outward region (a). This pressure gradient balances with the hoop stress in the outward region (a) because the centrifugal force is small near the upper wall. Second, in the inward region (b), the pressure gradient is weaker in the transition region than in the convective region [see Figs. 10(a) and 10(b)]. This is because the enhanced elastic force almost balances with the centrifugal force without the pressure gradient.

This section is summarized as follows [see also Fig. 12(b)]. The jet flow in the inward region (b) disappears, and another jet flow in the outward region (a) emerges because of the streamwise elastic force at the beginning of the transition region. Through the transition region, the jet flow gradually moves from the upper wall to the bottom wall because of the hoop stress.

3. Elastic region

In the elastic region, we can see the characteristic flow patterns that resemble the flow patterns observed in the convective region. The separation vortex is present in the outward region (a), and the jet flow is present near the bottom wall [see Figs. 4(a) and 4(c)]. Despite the similar appearance, the generation mechanism of the flow patterns in the elastic region is just different from that in the convective region because the convective term does not contribute to the generation of the flow patterns in the elastic region.

The generation mechanism of the separation vortex is as follows. From the transition region to the elastic region, a large-stress beltlike region is generated [see Figs. 11(d) and 11(e)]. Because the convective term merely varies with Wi, the pressure-gradient term grows with the elastic term (see Fig. 3). Then, the pressure also becomes large in this beltlike region [see Fig. 10(c)]. The pressure gradient inhibits the flow from the outward region (a) to the contraction region (c). Hence, the separation vortex emerges in the outward region (a) again. Note that the separation vortex appears in the low-pressure region unlike that in the convective region [see Figs. 10(a) and 10(c)].

In the elastic region, jet flows are present near the inward region (b) and the large-velocity region between the inward region (d) and the outward region (e) [see Fig. 10(f)]. The jet flow near the bottom wall is much broader than that in the convective region (see curves [a]–[c] and [f] in Fig. 5(a)) because the jet flow is induced in the broad large-elastic-stress region [see Fig. 11(e)]. The viscous drag in the elastic region is much smaller than that in the convective region (see Fig. 7) since the jet flow near the wall is broader. The growth rate of the flow rate becomes small with Wi in the elastic region. This is because the growth rate of the elastic stress also becomes small at sufficiently large Wi as shown in Fig. 9. This saturation stems from a large restoring effect with the large conformation tensor as formulated in Eqs. (3) and (5). We summarize this section as follows [see also Fig. 12(c)]. The separation vortex in the low-pressure region and the jet flow in the inward regions (b) emerge due to the large hoop stress and the streamwise elastic force in the elastic region.

In these sections, we have described the mechanism of the flow pattern transitions. We focus particularly on the separation vortices and the jet flows. The streamwise elastic force

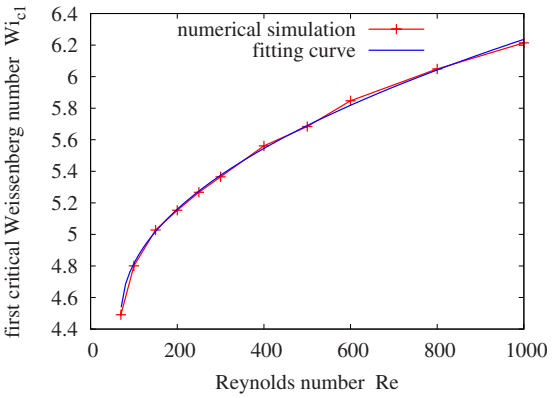

FIG. 13. (Color online) First critical Weissenberg number Wi_{c1} as a function of Re. The curve of Wi_{c1} is fitted with a power law $F_1(\mathrm{Re})=A_1(\mathrm{Re}-\mathrm{Re}_c)^{A_2}+A_3$, where $\mathrm{Re}_c=70$, $A_1\sim0.06$, $A_2\sim0.5$, and $A_3\sim4.5$.

and the change of balance among the elastic force and the other forces cause the transition of these flow patterns.

E. Scaling analysis on the elastic wall friction

In the previous section, we qualitatively described the mechanisms of the flow pattern transitions. In this section, we perform more quantitative analyses on the scaling relation of the elastic stress τ to the nondimensional parameters Wi and Re.

In Fig. 13, we show Wi_{c1} as a function of Re. The curve of Wi_{c1} is fitted with a power law $F_1(\mathrm{Re})=A_1(\mathrm{Re}-\mathrm{Re}_c)^{A_2}+A_3$, where Re_c is fixed to 70. The values of the fitting parameters are $A_1\sim0.06$, $A_2\sim0.5$, and $A_3\sim4.5$. The following relation:

$$\mathrm{Wi}_{c1}\propto\sqrt{\mathrm{Re}-\mathrm{Re}_c} \tag{21}$$

is nearly satisfied. $\mathrm{Re}_c=70$ is a reasonable value because the first transition is not apparently observed when $\mathrm{Re}<\mathrm{Re}_c$. Although we draw a line from Re=70 and Wi$\sim$4.5 to Re=0 and Wi=0 as the extension of Wi_{c1} in Fig. 2, the critical Re in the limit $\mathrm{Wi}\to0$ would be larger than zero in experiments.

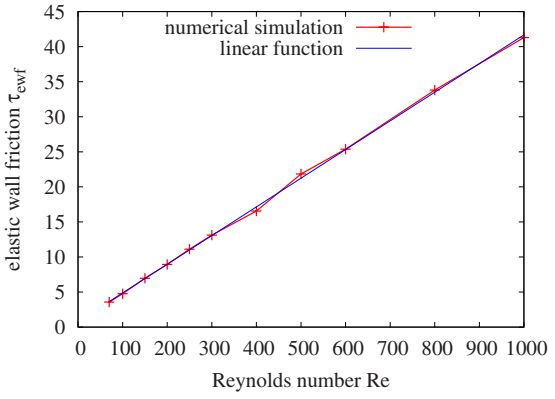

FIG. 14. (Color online) Elastic wall friction τ_{ewf} at Wi_{c1} as a function of Re. The line $\mathrm{F}_2=B_1(\mathrm{Re}-\mathrm{Re}_c)+B_2$, where $\mathrm{Re}_c=70$, $B_1=4.1\times10^{-2}$, and $B_2=3.6$, is superposed.

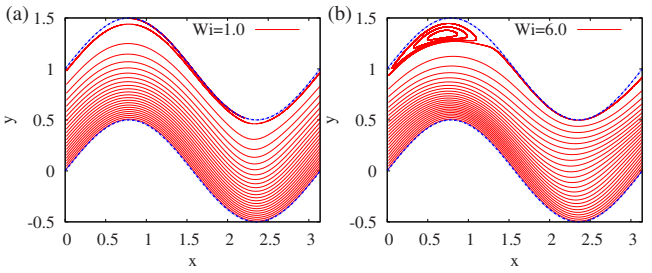

FIG. 15. (Color online) Streamlines of the steady solutions at the small Weissenberg number Wi=1.0 and the moderate Weissenberg number Wi=6.0 at Re=0.

The magnitude of the elastic term $\|\nabla\cdot\boldsymbol{\tau}\|$ is close to that of the convective term $\|\mathrm{Re}(\boldsymbol{u}\cdot\nabla)\boldsymbol{u}\|$ at Wi_{c1} as shown in Fig. 3. When we scale the nondimensional velocity and the derivatives to $O(1)$, the following relationship is derived:

$$\boldsymbol{\tau}\propto\mathrm{Re}. \tag{22}$$

Figure 14 shows the elastic wall friction τ_{ewf} at Wi_{c1} as a function of Re. We superpose the line $F_2=B_1(\mathrm{Re}-\mathrm{Re}_c)+B_2$, where $\mathrm{Re}_c=70$, $B_1=4.1\times10^{-2}$, and $B_2=3.6$ in Fig. 14. The linear relationship (22) between $\boldsymbol{\tau}$ and Re is indeed approximately satisfied. The two relations $\boldsymbol{\tau}\propto\mathrm{Re}-\mathrm{Re}_c$ and $\mathrm{Wi}_{c1}\propto\sqrt{\mathrm{Re}-\mathrm{Re}_c}$ lead to the following relationship between the elastic stress and Wi_{c1}:

$$\boldsymbol{\tau}\propto{\mathrm{Wi}_{c1}}^2. \tag{23}$$

F. Purely elastic limit

In this section, we show the flow patterns of purely elastic flows at Re=0. Recent years, purely elastic flows have been intensively studied in order to investigate elastic instability and elastic turbulence [3,10,13,18].

Figure 15 shows streamlines of the steady solutions at the low Weissenberg number Wi=1.0 and the moderate Weissenberg number Wi=6.0 at Re=0. The separation vortex is not observed at low Wi unlike the calculations at moderate Re (see Fig. 4). This is due to vanishing of the convective effect. When the convective term is zero, the centrifugal force also vanishes. Because the centrifugal force balances with the pressure gradient at low Wi, the pressure gradient also comparably becomes small. Then, the pressure gradient cannot inhibit the flows through the outward region (a), and hence the separation vortex is not induced in the outward region (a).

At moderate Wi, the elastic force and the pressure gradient are also dominant at Re=0 as observed at moderate Re. The flow pattern at Re=0 in Fig. 15(b) is indeed apparently similar to that at moderate Re in Fig. 4(c). At Re=0, Wi_{c2} is nearly close to Wi at which the separation vortex appears.

G. Poiseuille-type flows

In this section, we show the flow patterns of the steady Poiseuille-type flows driven by a body force in order to elucidate the dependence of the flow pattern transition on driving forces. We impose a constant body force (a constant pres-

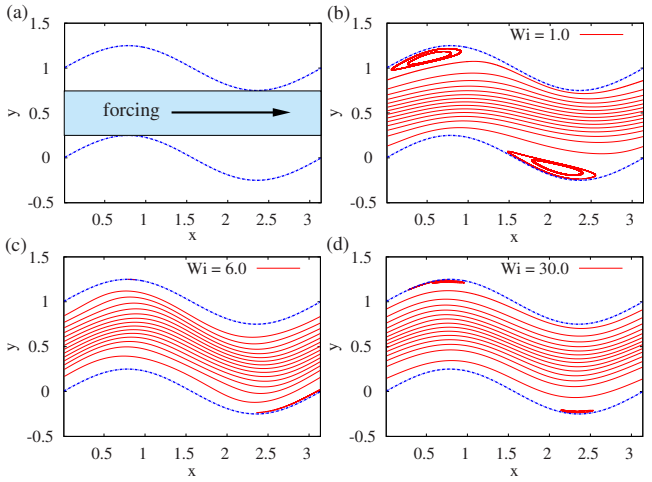

FIG. 16. (Color online) (a) Region in which a constant body force is imposed in Poiseuille-type flows. (b)–(d) Streamlines of Poiseuille-type flows at (b) Wi=1.0, (c) Wi=6.0, and (d) Wi =30.0 at Re=200.

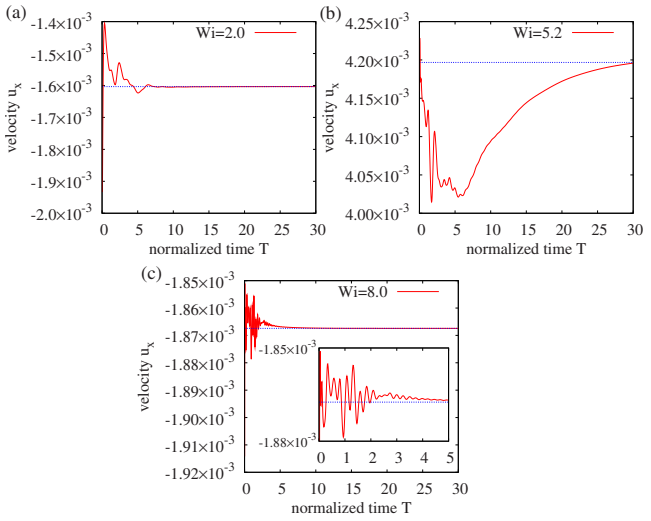

FIG. 17. (Color online) Relaxation processes of perturbations of velocity component u_x (a) in the convective region Wi=2.0, (b) in the transition region Wi=5.2, and (c) in the elastic region Wi=8.0. The inset of (c) shows the relaxation process magnified in the initial short period at Wi=8.0. Normalized time T is defined as $T=t/\mathrm{Wi}$. Horizontal lines denote the value of the velocity component u_x of initial conditions.

sure gradient) only in the rectangular region between the inlet and the outlet as shown in Fig. 16(a). In this method, the wall amplitude A needs to be less than the half width of the channel $A=0.5$. We adopt $A=0.3$ in the Poiseuille-type flow calculations instead of $A=0.5$ used in the Couette-type flow ones. The magnitude of the body force is determined, so that the flow rate FR is nearly fixed at every Wi.

Figures 16(b)–16(d) show streamlines of the steady solutions of the Poiseuille-type flows at Re=200 at the low Weissenberg number Wi=1.0, at the moderate Weissenberg number Wi=6.0, and at the high Weissenberg number Wi=30.0, respectively. There are two separation vortices in the outward regions (a) and (e) at Wi=1.0. These separation vortices disappear at Wi=6.0 and reappear at Wi=15.0. These vortices grow slowly with increasing Wi when Wi$>$15.0.

This result shows that in Poiseuille-type flows we can observe flow pattern transitions qualitatively similar to those in Couette-type flows. However, the Weissenberg numbers at which the separation vortex appears and disappears are different between the two flows.

As well as the difference in the driving force, the quantitative difference may be also caused by the decrease in the wall amplitude A. In Couette-type flows at Re=200 with A =0.3, the separation vortex disappears nearly at Wi=7.0 and reappears nearly at Wi=8.5. These Weissenberg numbers are larger than those with $A=0.5$ because the elastic force with $A=0.3$ is smaller than that with $A=0.5$ at the same Wi for the reason that the curvature and the contraction of the channel are smaller with $A=0.3$ than with $A=0.5$. However, the Weissenberg number at which the separation vortex reappears is still different between Couette-type flows (Wi =8.5) and Poiseuille-type flows (Wi=15.0) with the same wall amplitude.

This difference may be resulted from the difference in dominant regions of a centrifugal (convective) force and an elastic force. In Poiseuille-type flows, the centrifugal force in the bulk region is larger than that near the walls, and the elastic force in the bulk region is smaller than that near the walls. In contrast, in Couette-type flows, the centrifugal force in the bulk region is smaller than that near the bottom wall, and the elastic force is large in both the inward regions near the walls and the contraction regions in the bulk flow. The difference may show that the flow pattern transition occurs with different mechanisms in the two-type flows.

V. DISCUSSION AND CONCLUDING REMARKS

In this study, we have sought base steady solutions of wavy-walled channel shear flows. However, a relaxation process to the steady solution is also important when we consider elastic instabilities of the base solutions. In this section, we discuss the relaxation process by analyzing relaxation times of perturbations.

In Fig. 17, we show relaxation processes of the velocity component u_x in the convective region Wi=2.0, the transition region Wi=5.2, and the elastic region Wi=8.0 at Re =200. The time is normalized with Wi, which is proportional to the relaxation time of the conformation tensor [see Eqs. (3) and (7)]. We impose the same perturbation on the initial conformation tensor in the three regions. Then, the velocity is also perturbed due to the coupling between the velocity and the conformation tensor.

This figure shows that the relaxation time and the perturbation amplitude are the largest in the transition region. We consider that the pressure gradient plays a key role in the difference of the relaxation processes. In the convective and elastic regions, the pressure gradient is comparable to the centrifugal force and the elastic force, respectively. In contrast, the pressure gradient in the transition region is relatively small (see Fig. 3). This may indicate that the pressure gradient suppresses the transfer of the stress perturbation to the velocity perturbation.

Note that the frequency of the oscillations is the largest in the elastic region as shown in the inset of Fig. 17(c). The oscillatory nature at large Wi is also observed in the earlier two-dimensional calculations of viscoelastic extensional flows [18].

We can consider several situations in which the perturbation would be sustained. First, the pressure may hardly suppress spanwise secondary flows for the lack of the degree of freedom in three-dimensional channels. Spanwise secondary flows (e.g., Görtler vortices) have been actually observed in three-dimensional curved-wall flows [43]. Second, subcritical instabilities may occur against certain finite-amplitude perturbations in wavy-walled channels as in the earlier studies of plane-Poiseuille flows [33,44]. The most unstable modes derived in linear stability analyses are candidates of the perturbations [45].

Finally, we summarize this study. We have numerically investigated laminar steady viscoelastic flows in canonical wavy-walled channels at moderate Re and Wi with a spectral element method. We found three types of steady solutions called convective, transition, and elastic. The separation vortex and the jet flow characterize the difference of the three solutions. The separation vortex in curved flows has been observed in numerical simulations and experiments of both Newtonian and non-Newtonian flows in wavy-walled channels [42,46].

When the flow pattern changes at the beginning of the transition region, the viscous wall friction greatly drops. Such drag reduction in laminar flows has been observed in experiments and numerical simulations of viscoelastic fluids in curved pipes [41,47].

The flow pattern transition is also accompanied with the sudden growth of the elastic wall friction. The growth mechanism of the elastic wall friction is similar to that of the wall friction due to the Reynolds stress intensified near walls in Newtonian turbulent flows. The similarity between laminar non-Newtonian flows and turbulent Newtonian flows has been already pointed out and analyzed [12,17,48].

We qualitatively described the mechanism of the flow pattern transition by considering the force balance among the centrifugal force, the elastic force, and the pressure gradient and the change of dominant terms in the Navier-Stokes equation. At every Wi, the streamwise elastic force as well as the hoop stress contributes to the flow pattern transition.

We quantitatively analyzed the force balance with a scaling analysis. We derived $\tau \propto \mathrm{Re}$ when the convective and elastic terms are comparable at Wi_{c1}. The critical Reynolds number $\mathrm{Re}_c \sim 70$ obtained in the scaling analysis is reasonable as a characteristic value at which a convective effect becomes effective [13].

We also performed the computations of purely elastic flows at $\mathrm{Re}=0$. Due to vanishing of the centrifugal force, the separation vortex is not present at low Wi, although it appears at moderate Wi. Note that Wi at which the separation vortex emerges in this study is close to Wi at which an elastic turbulence sets in at $\mathrm{Re} \ll 1$ in the experiments of viscoelastic flows in wavy-wall channels [12].

We finally performed the computations of Poiseuille-type flows driven by a constant body force. The flow pattern transitions are also observed in the Poiseuille-type flows as in the Couette-type flows.

ACKNOWLEDGMENTS

I gratefully acknowledge Sadayoshi Toh for essential discussions. Takeshi Matsumoto, Shunsuke Kohno, and all members of our laboratory provided us with much help, advice, and comments in the preparation of the manuscript. This work was supported by the Grant-in-Aid for the Global COE Program "The Next Generation of Physics, Spun from Universality and Emergence" from the Ministry of Education, Culture, Sports, Science and Technology (MEXT) of Japan. The numerical calculations were carried out on SX8 and Altix at YITP in Kyoto University and SX-8 at CMC in Osaka University.

[1] R. B. Bird, C. F. Curtiss, R. C. Armstrong, and O. Hassager, *Dynamics of Polymeric Liquids*, Fluid Mechanics Vol. 1, 2nd ed. (Wiley, New York, 1987).
[2] K. Weissenberg, Nature (London) **159**, 310 (1947).
[3] R. G. Larson, E. S. G. Shaqfeh, and S. J. Muller, J. Fluid Mech. **218**, 573 (1990).
[4] A. Groisman and V. Steinberg, Phys. Fluids **10**, 2451 (1998).
[5] A. Groisman and V. Steinberg, Phys. Rev. Lett. **77**, 1480 (1996).
[6] B. M. Baumert and S. J. Muller, J. Non-Newtonian Fluid Mech. **83**, 33 (1999).
[7] D. G. Thomas, R. Sureshkumar, and B. Khomami, Phys. Rev. Lett. **97**, 054501 (2006).
[8] Y. L. Joo and E. S. G. Shaqfeh, Phys. Fluids A **4**, 524 (1992).
[9] G. H. McKinley, J. A. Byars, R. A. Brown, and R. C. Armstrong, J. Non-Newtonian Fluid Mech. **40**, 201 (1991).
[10] P. Pakdel and G. H. McKinley, Phys. Rev. Lett. **77**, 2459 (1996).
[11] A. Groisman and V. Steinberg, Nature (London) **405**, 53 (2000).
[12] A. Groisman and V. Steinberg, Nature (London) **410**, 905 (2001).
[13] A. Groisman and V. Steinberg, New J. Phys. **6**, 29 (2004).
[14] T. Burghelea, E. Segre, and V. Steinberg, Phys. Rev. Lett. **92**, 164501 (2004).
[15] T. M. Squires and S. R. Quake, Rev. Mod. Phys. **77**, 977 (2005).
[16] J. A. Pathak, D. Ross, and K. B. Migler, Phys. Fluids **16**, 4028 (2004).
[17] S. Berti, A. Bistagnino, G. Boffetta, A. Celani, and S. Musacchio, Phys. Rev. E **77**, 055306(R) (2008).
[18] B. Thomases and M. Shelley, Phys. Rev. Lett. **103**, 094501 (2009).
[19] K. J. Cho, M. Kim, and H. D. Shin, Fluid Dyn. Res. **23**, 349 (1998).
[20] Y. L. Joo and E. S. G. Shaqfeh, Phys. Fluids A **4**, 2415 (1992).

[21] M. Renardy and Y. Renardy, J. Non-Newtonian Fluid Mech. **22**, 23 (1986).
[22] N. Fiétier and M. O. Deville, J. Comput. Phys. **186**, 93 (2003).
[23] E. Abu-Ramadan and R. E. Khayat, Int. J. Numer. Methods Fluids **51**, 117 (2006).
[24] R. B. Bird, P. J. Dotson, and N. L. Johnson, J. Non-Newtonian Fluid Mech. **7**, 213 (1980).
[25] A. Peterlin, J. Polym. Sci., Part B: Polym. Lett. **4**, 287 (1966).
[26] M. D. Chilcott and J. M. Rallison, J. Non-Newtonian Fluid Mech. **29**, 381 (1988).
[27] D. F. James, Annu. Rev. Fluid Mech. **41**, 129 (2009).
[28] R. Sureshkumar, A. N. Beris, and R. A. Handler, Phys. Fluids **9**, 743 (1997).
[29] T. Vaithianathan and L. R. Collins, J. Comput. Phys. **187**, 1 (2003).
[30] K. A. Kumar and M. D. Graham, J. Fluid Mech. **443**, 301 (2001).
[31] A. W. El-Kareh and L. G. Leal, J. Non-Newtonian Fluid Mech. **33**, 257 (1989).
[32] R. Sureshkumar and A. N. Beris, J. Non-Newtonian Fluid Mech. **60**, 53 (1995).
[33] K. Atalik and R. Keunings, J. Non-Newtonian Fluid Mech. **102**, 299 (2002).
[34] R. G. Owens and T. N. Phillips, *Computational Rheology* (Imperial College Press, London, 2002).
[35] A. T. Patera, J. Comput. Phys. **54**, 468 (1984).
[36] C. Canuto, M. Y. Hussaini, A. Quarteroni, and T. A. Zang, *Spectral Methods: Evolution to Complex Geometries and Applications to Fluid Dynamics* (Springer, New York, 2007).
[37] J. P. Boyd, *Chebyshev and Fourier Spectral Methods*, 2nd ed. (Dover, New York, 2001).
[38] Y. Maday and A. T. Patera, in *State-of-the-Art Surveys on Computational Mechanics*, edited by A. K. Noor and J. T. Oden (ASME, New York, 1989), p. 71.
[39] Y. Maday, D. Meiron, A. T. Patera, and E. M. Rønquist, SIAM J. Sci. Comput. (USA) **14**, 310 (1993).
[40] R. G. Owens and T. N. Phillips, Int. J. Numer. Methods Eng. **39**, 1517 (1996).
[41] Y. Fan, R. I. Tanner, and N. Phan-Thien, J. Fluid Mech. **440**, 327 (2001).
[42] Y. Asako, H. Nakamura, and M. Faghri, Int. J. Heat Mass Transfer **31**, 1237 (1988).
[43] W. S. Saric, Annu. Rev. Fluid Mech. **26**, 379 (1994).
[44] A. N. Morozov and W. van Saarloos, Phys. Rep. **447**, 112 (2007).
[45] B. Meulenbroek, C. Storm, A. N. Morozov, and W. van Saarloos, J. Non-Newtonian Fluid Mech. **116**, 235 (2004).
[46] K. Arora, R. Sureshkumar, and B. Khomami, J. Non-Newtonian Fluid Mech. **108**, 209 (2002).
[47] W. M. Jones and O. H. Davies, J. Phys. D: Appl. Phys. **9**, 753 (1976).
[48] C. G. Speziale, Annu. Rev. Fluid Mech. **23**, 107 (1991).